NANO LETTERS

2009
Vol. 9, No. 12
3968-3973

Single-Molecule Electrocatalysis by Single-Walled Carbon Nanotubes

Weilin Xu, Hao Shen, Yoon Ji Kim, Xiaochun Zhou, Guokun Liu, Jiwoong Park, and Peng Chen*

Department of Chemistry and Chemical Biology, Cornell University, Ithaca, New York 14853

Received March 29, 2009

ABSTRACT

We report a single-molecule fluorescence study of electrocatalysis by single-walled carbon nanotubes (SWNTs) at single-reaction resolution. Applying super-resolution optical imaging, we find that the electrocatalysis occurs at discrete, nanometer-dimension sites on SWNTs. Single-molecule kinetic analysis leads to an electrocatalytic mechanism, allowing quantification of the reactivity and heterogeneity of individual reactive sites. Combined with conductivity measurements, this approach will be powerful to interrogate how the electronic structure of SWNTs affects the electrocatalytic interfacial charge transfer, a process fundamental to photoelectrochemical cells.

Owing to their unique structural, mechanical, and electronic properties, carbon nanotubes (CNTs), especially single-walled carbon nanotubes (SWNTs), have gained wide applications, such as in nanoelectronics, sensing, catalysis, and energy harvesting.[1−17] Their nanometer size and good conductivity also attracted their applications in electrochemistry and electrocatalysis,[8,18−22] for which their nanometer dimension enhances the mass transport rate, so fast electrochemical charge-transfer kinetics may be studied.[19,20,23]

Currently, preparation of SWNTs always generates nanotubes of variable chirality.[2,3,7,13,17] Obtaining monodisperse SWNTs remains a persistent challenge. As the chirality of SWNTs determines their electronic properties (e.g., metallic or semiconducting), individual SWNTs can have different electrochemical and electrocatalytic properties.[19,20,23] To circumvent this polydispersion obstacle, individual CNTs/SWNTs have been used as electrodes to study their electrochemical properties, where the electrochemical current going through a single nanotube is measured with high sensitivity.[18−20] For electrocatalysis studies, measuring electrical currents, although powerful in interrogating the property of a particular CNT/SWNT, cannot differentiate electrocatalytic reactions that occur at different locations on the nanotube, if the sidewall, tube ends, or defect sites have different catalytic properties. Differentiating reactions spatially is important however as recent studies have shown that defect sites or exogenous atoms on the nanotube may render CNTs special catalytic activities.[9,24−27] Furthermore, electrical current measurements typically can only be performed on one nanotube at a time, limiting the data throughput. Multiplexed observations of CNT-mediated electrochemistry or electrocatalysis are thus highly desired.

Single-molecule fluorescence microscopy, with its capability of multiplexed observation and its nanometer spatial resolution from the super-resolution imaging approach,[28−36] offers an alternative to study electrochemical and electrocatalytic reactions of individual CNTs, if suitable fluorescent reporters are available. Pioneering work in single-molecule spectroelectrochemistry[37,38] has been done on polymer nanoparticles,[37,39,40] metal nanoparticles,[41] fluorescent redox-active molecules,[42] and clay nanoparticles.[43] Here we report using single-molecule fluorescence microscopy to study the electrocatalysis by SWNTs. By designing a fluorogenic reaction electrocatalyzed by SWNTs and detecting a fluorescent product at the single-molecule level with total internal reflection microscopy, we achieve real-time *multiplexed* observation of SWNT electrocatalysis at the single-reaction, single-reactive-site level with nanometer spatial resolution.

Our fluorogenic reaction is based on the well-known two-stage electro-reduction of the nonfluorescent molecule resazurin in aqueous solution (Figure 1A).[44] The first stage reduces resazurin (**S**) irreversibly to the fluorescent resorufin (**P**); the second stage reduces resorufin to the nonfluorescent dihydroresorufin ($\mathbf{PH_2}$) and is reversible. The intense fluorescence of resorufin enables its ready detection at the single-molecule level, as shown previously in studying the chemical catalysis by individual metal nanoparticles.[45−47]

To test that SWNTs can indeed electrocatalyze these transformations, we performed cyclic voltammetry (CV) of **S** using indium tin oxide (ITO)-coated quartz as the working electrode with SWNTs deposited on top. The optical transparency of ITO makes it suitable for fluorescence

* To whom correspondence should be addressed. E-mail: pc252@cornell.edu.

10.1021/nl900988f CCC: $40.75
Published on Web 04/14/2009

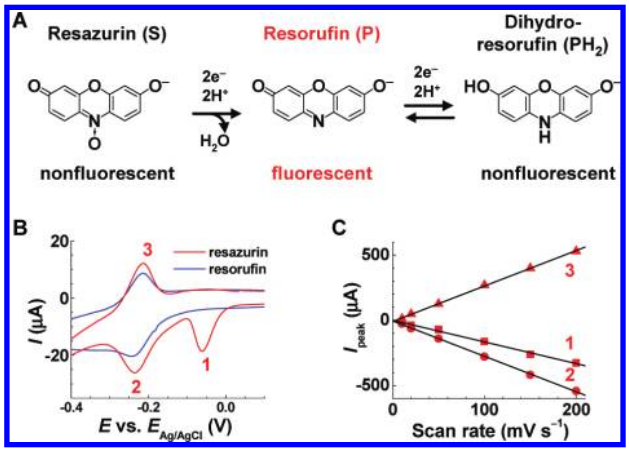

Figure 1. SWNTs-electrocatalyzed redox of resazurin. (A) Redox chemistry of resazurin in aqueous solutions. (B) Cyclic voltammograms of 50 μM resazurin or resorufin in 50 mM pH 7.3 phosphate buffer with a SWNT-coated ITO electrode at the 10 mV s^{-1} scan rate. (C) Scan rate dependence of the peak currents in (B). Lines are linear fits.

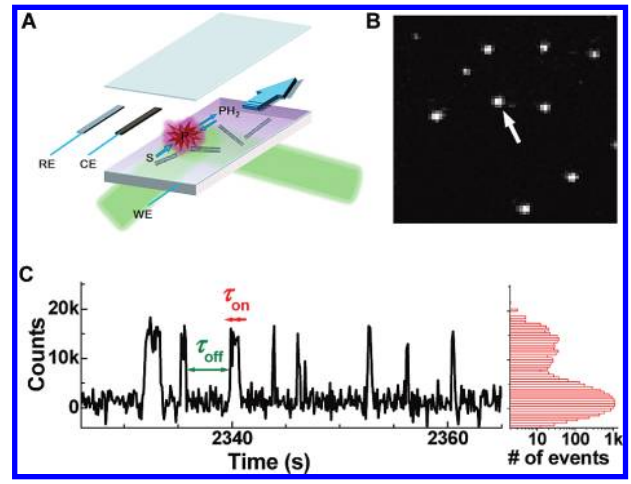

Figure 2. Real-time single-molecule detection of SWNT electrocatalysis. (A) Experimental design using an electrochemical flow cell made between an ITO-coated quartz slide and a coverslip, and total internal reflection fluorescence microscopy. WE, RE, CE: working, reference, counter electrodes. (B) Fluorescence image ($\sim$17 $\times$ 19 μm^2) of SWNT electrocatalysis at $-$0.35 V with 0.05 μM resazurin in phosphate buffer. Taken at 100 ms frame rate. (C) Left: segment of the fluorescence trajectory from the fluorescence spot marked by the arrow in (B). Right: histogram of an 18 min long trajectory.

microscopy experiments (see below). The CV of **S** shows two reduction peaks and one oxidation peak in the range of $-$0.5 to 0.5 V, as expected (Figure 1B and Supporting Information, Figure S1). (All potentials cited in this study are referenced to the Ag/AgCl electrode.) The first reduction peak does not have a corresponding oxidation peak and can be assigned as the irreversible **S** $\rightarrow$ **P** electro-reduction. Consistently, fluorescence spectra of the reaction solution show the accumulation of **P** after repeated CV scans (Supporting Information, Figure S2). The second reduction peak and the oxidation peak coincide with those in the CV of pure **P** (Figure 1B); they can thus be assigned as the reversible **P** $\leftrightarrow$ **PH_2** redox. Their peak separation (32 mV) at low scan rates further supports their assignments as reversible two-electron redox processes.[23] Additionally, in the CV of **S**, all three peak-currents show a linear dependence on the scan rate of electric potential (Figure 1C), indicating that these redox processes result from SWNT surface adsorbed molecules.[23]

Many control experiments support that SWNTs are responsible for the observed electrocatalysis of **S** redox. (1) No appreciable redox is observed by CV in the same potential range in the absence of either **S** or SWNTs (Supporting Information, Figure S3). (2) All final experiments were performed on SWNTs that have been purified using acid treatment to remove as much metal nanoparticle catalysts as possible[48] and using centrifugation to remove amorphous carbon and carbon nanoparticles (Supporting Information, Section II.4).[49] Compared with the unpurified SWNTs, the electrocatalytic activity of the purified SWNTs is higher (Supporting Information, Figure S4C), supporting that the observed electrocatalysis is due to SWNTs and not impurities such as metal nanoparticles, amorphous carbon, or carbon nanoparticles. (3) When studied separately by CV, iron nanoparticles, the only significant metal catalyst residual identified in our sample (Supporting Information, Figure S4A), and copper nanoparticles, another possible metal residual according to the supplier, do not show electrocatalytic activity in **S** reduction (Supporting Information, Figure S5). (4) The purified SWNTs have higher electrocatalytic activity per unit mass than carbon black (Supporting Information, Figure S6); therefore, the observed electrocatalytic activity of purified SWNTs cannot be mainly due to the residual amorphous carbon or carbon particle impurities, as the amount of these impurities is small.

To monitor the electrocatalysis by SWNTs at the single-molecule level, we used an electrochemical flow cell and a wide-field total internal reflection fluorescence microscope (Figure 2A). We deposited well-sonicated, diluted SWNT suspensions onto an ITO-coated quartz slide, which acts as the working electrode, and flowed on top the solution containing **S** at a constant flow rate (Supporting Information). A Ag/AgCl reference electrode and a Pt counter electrode were also placed in the flow cell. The applied potential on the ITO-working electrode can effectively change the chemical potential of SWNTs due to their small quantum capacitances.[19,20,50] Atomic force microscopy shows that individual SWNTs can be well dispersed, although SWNT bundles might also be present on the surface (Supporting Information, Figure S7).

Upon applying a constant negative potential (i.e., under steady-state electrocatalytic reaction conditions), we recorded movies of stochastic fluorescence bursts at many localized spots on the ITO surface under 532 nm laser illumination (Supporting Information, Movie S1); each spot gives out fluorescence bursts repetitively. A typical image from such a movie contains many fluorescence spots of diffraction-limited size (fwhm $\sim$ 400 nm, Figure 2B). A typical time trajectory of fluorescence intensity from one of these fluorescence spots contains stochastic two-state off-on signals (Figure 2C and Supporting Information, Figure S8). The digital, two-state nature of these fluorescence trajectories

indicates that each burst comes from a single **P** molecule; were it from many molecules, the trajectory would have variable number of intensity states depending on the number of molecules. As no digital fluorescence trajectories were observed in the absence of applied potential, **S**, or SWNTs, we attributed the single-**P** fluorescence bursts to electrocatalytic reductions of **S** by SWNTs.

The spatial localization of the fluorescence bursts within diffraction-limited spots suggests that the reactions occur at discrete sites rather than on the entire sidewall of the SWNTs, as each SWNT is many microns long. These reactive sites can be defect sites or nanotube ends.[9] To resolve the dimension of these reactive sites beyond diffraction-limited resolution, we applied the optical super-resolution imaging method,[28−36] as in photoactivation localization microscopy (PALM)[30,32] and stochastic optical reconstruction microscopy (STORM).[31,35,51,52] These super-resolution microscopy techniques utilize two features of single-molecule fluorescence detection to achieve subdiffraction imaging resolution: (1) The nanometer accuracy in localizing the center of the emission point spread function (PSF) of a single fluorescent molecule in a wide-field image, provided that a large number of fluorescence photons are detected.[53,54] (2) Temporal separation of fluorescence detection of individual molecules that reside within the diffraction-limited resolution (∼a few hundred nanometers). This temporal separation is manifested by the off-on signals in the fluorescence intensity trajectories and can be achieved through photoinduced switching of fluorescent molecules as in PALM and STORM, or, as in the SWNT electrocatalysis here, through electrocatalytic generation of individual fluorescent **P** molecules (Figure 2C).

Figure 3A shows a conventional wide-field fluorescence image of a single **P** molecule at a SWNT reactive site during one τ_{on} period; the fluorescence intensity spreads over a few pixels as a PSF (each pixel = 267 nm). Fitting this PSF with a two-dimensional Gaussian function localizes its center position to ±4.5 nm accuracy (Figure 3B, and see Supporting Information Section I.5 for the determination of center localization accuracy). The center localizations from fitting the PSFs of many τ_{on} periods (i.e., many **P** molecules) in one fluorescence trajectory show a spread (Figure 3C), and they follow a Gaussian distribution.[31,35,51,52] The fwhm of the localization distributions from many reactive sites gives our spatial resolution of ∼20 nm (Figure 3D), comparable to those in PALM and STORM imaging[30−32,35,51,52] and an order of magnitude higher than the resolution (∼400 nm) in the diffraction-limited wide-field fluorescence image (Figure 3A). Considering the diameters of these SWNTs are about 1 ± 0.3 nm,[55] these reactive sites on the SWNTs should thus be no more than ∼1 × 20 nm^2 in dimension. Therefore, each reactive site here acts as an ultrasmall electrode, whose nanometer dimension offers efficient mass transport, allowing the study of electrocatalytic electron-transfer kinetics at low reactant concentrations.

In the single-molecule electrocatalysis fluorescence trajectories (Figure 2C), each sudden intensity increase corresponds to an electrocatalytic formation of a single **P** at a SWNT reactive site (the actual chemical transformation occurs on

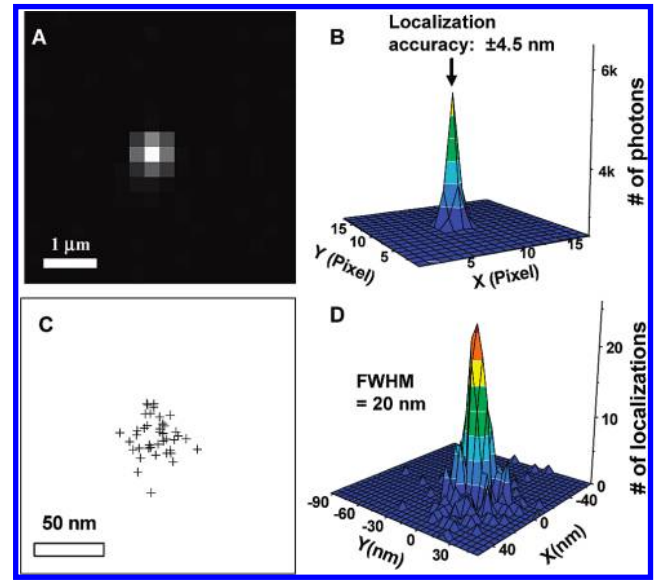

Figure 3. Super-resolution imaging of SWNT reactive sites. (A) Conventional wide-field fluorescence image of a single resorufin at a reactive site during one τ_{on} period. Pixel size = 267 nm. A surface plot of this image depicting the PSF is shown in Supporting Information, Figure S9A. (B) Two-dimensional Gaussian fit to the PSF function in panel A. The fwhm of the fit is ∼410 nm. The center localization is determined to ±4.5 nm. (C) Center localizations determined from the many τ_{on} periods of one single-molecule electrocatalysis fluorescence trajectory. (D) Two-dimensional histogram of the center localizations. Gaussian fit gives fwhm ∼20 nm (Supporting Information, Figures S9B,C). To increase statistics, the localizations from 25 reactive sites are combined, and the center of mass of the localizations from each reactive site was used for alignment, as done in STORM imaging.[51]

the subpicosecond time scale and cannot be resolved here). For the sudden intensity decreases, they could be due to (1) photobleaching of **P**; (2) fluorescence blinking of **P**; (3) **P** dissociation from the SWNT, as **P** in solution is undetectable at our imaging condition due to its fast diffusion; or (4) electro-reduction of **P** to $\mathbf{PH_2}$. Under similar laser excitations, control experiments show that the average photobleaching time of a single **P** molecule is ∼17 s and the average blinking on-time is ∼5 s (Supporting Information, Figure S10), both much longer than the average τ_{on} in the fluorescence trajectories (about hundreds of milliseconds, see also Figure 5A below). Therefore, **P** photobleaching and blinking do not contribute significantly to the single-molecule fluorescence trajectories of SWNT electrocatalysis.

To determine the time scale of **P** dissociation from SWNTs, we performed ensemble fluorescence microscopy of electrocatalysis by aggregates of SWNTs. Using an electrochemical flow cell as in our single-molecule electrocatalysis experiments, we deposited on the ITO surface much larger amount of SWNTs, many of which form aggregates. With a constant flow of 0.1 μM **S** solution, we rapidly applied a negative step potential (−0.15 V), which was switched off after 3 s. Upon applying the negative potential, many **S** molecules are electrocatalytically reduced to **P** on the SWNTs, leading to an increase of fluorescence intensity. Figure 4A shows an image of the fluorescence during the time the potential is on; the fluorescence intensity covers an area of ∼8 × 8 μm^2 where

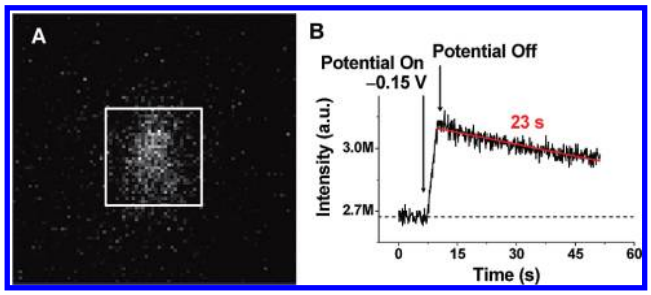

Figure 4. Ensemble fluorescence microscopy of SWNT electrocatalysis. (A) Fluorescence image (24 × 24 μm^2) of electrocatalysis by aggregates of SWNTs at 0.1 μM resazurin in 50 mM pH 7.3 phosphate buffer. Image taken at 100 ms frame rate. (B) Time profile of the fluorescence intensity over an 8 × 8 μm^2 bright area in (A) (boxed). The red line is an exponential decay fit to the decay region of the fluorescence intensity profile. The dashed horizontal line indicates the background level.

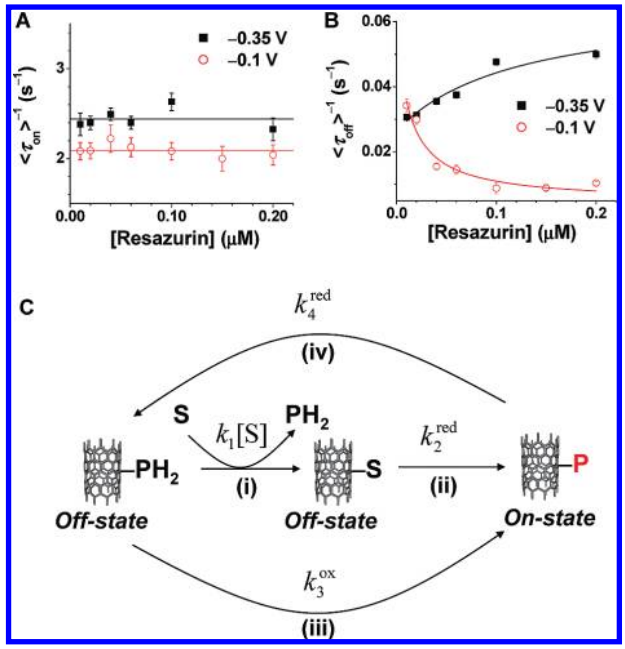

Figure 5. Kinetic mechanism of SWNT electrocatalysis. (A, B) Resazurin concentration dependence of $\langle\tau_{on}\rangle^{-1}$ and $\langle\tau_{off}\rangle^{-1}$ at two different potentials. For each potential, the data are averaged over the fluorescence trajectories of >50 reactive sites. Error bars in the graphs are standard error of the mean (SEM). Solid lines are fits of eqs 1 and 2; for −0.35 V, $k_1 = 0.5 \pm 0.3$ $\mu M^{-1}s^{-1}$, $k_2^{red} = 0.07 \pm 0.01$ s^{-1}, $k_3^{ox} = 0.026 \pm 0.003$ s^{-1}, $k_4^{red} = 2.4 \pm 0.1$ s^{-1}; for −0.1 V, $k_1 = 0.3 \pm 0.5$ $\mu M^{-1}s^{-1}$, $k_2^{red} = 0.004 \pm 0.003$ s^{-1}, $k_3^{ox} = 0.06 \pm 0.02$ s^{-1}, $k_4^{red} = 2.1 \pm 0.1$ s^{-1}; errors here are standard deviation (SD). Note the values here represent the averaged properties of many SWNT reactive sites. (C) Kinetic mechanism of the SWNT electrocatalysis. The fluorescence state (on or off) is indicated at each stage of the reaction. **S**, resazurin; **P**, resorufin; **PH_2**, dihydroresorufin.

aggregates of SWNTs reside. Upon switching off the potential, no further electrocatalysis occurs, and the fluorescence intensity decreases gradually due to dissociation of **P** from the SWNTs. (Photobleaching of **P** in this ensemble microscopy experiment is insignificant here, as the laser intensity used is only about one-fourth of that used in single-molecule electrocatalysis experiments.) Figure 4B shows the time profile of the fluorescence intensity; the rapid fluorescence increase is clear and it results from the formation of **P** upon turning on the potential, and so is the gradual decrease of fluorescence that results from **P** dissociation upon turning off the potential. Fitting the part of the fluorescence decrease with an exponential decay function, we obtained a time constant of ~23 s, which is the time scale of **P** dissociation from the SWNTs. This time scale is much longer than the average τ_{on} in the single-molecule electrocatalysis fluorescence trajectories (Figure 2C). Taking into account of the control experiments on **P** photobleaching and blinking, we thus attributed the sudden intensity decreases in the single-molecule fluorescence trajectories to electro-reduction events of **P** to **PH_2**.

In the single-molecule fluorescence trajectories (Figure 2C), the waiting times, τ_{on} and τ_{off}, are the two most important observables. Resolving them enables us to probe the kinetic mechanism of the electrocatalysis in two parts separately: τ_{on} is the waiting time for electro-reduction of **P** to **PH_2** after a **P** molecule is formed at a reactive site; τ_{off} is the waiting time for **P** formation. Their individual values are stochastic, but their statistical properties, such as average values and distributions, are well-defined by the underlying reaction kinetics. Statistically, $\langle\tau_{on}\rangle^{-1}$ and $\langle\tau_{off}\rangle^{-1}$, where $\langle\ \rangle$ denotes averaging, represent the time-averaged single-site rates of **P** to **PH_2** reduction and of **P** formation, respectively. When averaged over the fluorescence trajectories from many reactive sites, $\langle\tau_{on}\rangle^{-1}$, the **P** reduction rate, is essentially independent of **S** concentration ([**S**]) regardless of the applied potential (Figure 5A). In contrast, $\langle\tau_{off}\rangle^{-1}$, the **P** formation rate, shows variable behaviors depending on the applied potential (Figure 5B); at −0.35 V, $\langle\tau_{off}\rangle^{-1}$ increases with increasing [**S**] and saturates, and at −0.1 V, $\langle\tau_{off}\rangle^{-1}$ decreases with increasing [**S**] and then flattens.

The [**S**]-independent nature of $\langle\tau_{on}\rangle^{-1}$ can be described by a simple **P** → **PH_2** electro-reduction reaction at a SWNT reactive site (Figure 5C, reaction (iv)). With the rate constant of this electro-reduction being k_4^{red}, the probability density function $f_{on}(\tau)$ of τ_{on} follows an exponential distribution,[56,57] $f_{on}(\tau) = k_4^{red} \exp(-k_4^{red}\tau)$; $\langle\tau_{on}\rangle^{-1}$ is

$$\langle\tau_{on}\rangle^{-1} = 1/\int_0^\infty \tau f_{on}(\tau)d\tau = k_4^{red} \quad (1)$$

Equation 1 is obviously independent of [**S**], consistent with experimental results (Figure 5A). As **P** → **PH_2** is an electro-reduction reaction, its rate constant k_4^{red} (and thus $\langle\tau_{on}\rangle^{-1}$) should be dependent on potential and increases with larger negative potential, as observed experimentally (Figure 5A).

To account for the variable [**S**]-dependence of $\langle\tau_{off}\rangle^{-1}$ at different potentials, we considered a **P** formation pathway that involves a substitution reaction of **PH_2** by **S** at the reactive site followed by electrocatalytic reduction of **S** to **P** (Figure 5C, reactions (i) and (ii)), as well as a pathway of direct oxidation of **PH_2** to **P** (reaction (iii)). The oxidation pathway is possible because **P** ↔ **PH_2** redox is reversible (Figure 1A). (See Supporting Information, Sections II.11 and II.12 for more discussions on the kinetic mechanism of the τ_{off} process.) With these two parallel pathways and following a single-molecule kinetic analysis (Supporting Information, Section II.11),[56,57] the equation connecting $\langle\tau_{off}\rangle^{-1}$ with the kinetic rate constants is

$$\langle\tau_{off}\rangle^{-1} = 1/\int_0^\infty \tau f_{off}(\tau)d\tau = \frac{k_2^{red}(k_3^{ox} + k_1[S])}{k_2^{red} + k_1[S]} \qquad (2)$$

where $f_{off}(\tau)$ is the probability density function of τ_{off}, k_1 is the rate constant of $\mathbf{PH_2}$ substitution by **S** at the reactive site (reaction (i)), k_2^{red} is the rate constant of electro-reduction of **S** to **P** (reaction (ii)), and k_3^{ox} is the rate constant of electro-oxidation of $\mathbf{PH_2}$ to **P** (reaction (iii)). When [**S**] $\rightarrow$ 0, $\langle\tau_{off}\rangle^{-1} \rightarrow k_3^{ox}$, because no **S** is available to replace $\mathbf{PH_2}$ and direct oxidation of $\mathbf{PH_2}$ to **P** dominates; when [**S**] is large, $\langle\tau_{off}\rangle^{-1} \rightarrow k_2^{red}$, because high [**S**] drives the substitution of $\mathbf{PH_2}$ by **S**, which is subsequently electro-reduced to **P**. Equation 2 predicts the variable [**S**]-dependences of $\langle\tau_{off}\rangle^{-1}$ at different potentials (Figure 5B). At more negative potentials (e.g., at −0.35 V) so that electro-reduction is more favorable than electro-oxidation (i.e., $k_2^{red} > k_3^{ox}$), $\langle\tau_{off}\rangle^{-1}$ increases asymptotically with increasing [**S**]. At less negative potentials (e.g., at −0.1 V) so that electro-oxidation is more favorable (i.e., $k_2^{red} < k_3^{ox}$), $\langle\tau_{off}\rangle^{-1}$ decreases asymptotically with increasing [**S**]. At an intermediate potential so that k_2^{red} and k_3^{ox} are approximately equal, $\langle\tau_{off}\rangle^{-1}$ would be independent of [**S**] (data not shown).

With eqs 1 and 2, we determined the kinetic constants, k_1, k_2^{red}, k_3^{ox}, and k_4^{red} for each reactive site by fitting its [**S**]-titration of $\langle\tau_{on}\rangle^{-1}$ and $\langle\tau_{off}\rangle^{-1}$. These kinetic constants quantify the reactivity of the reactive site in the corresponding reactions. Figure 6A,F shows the data and fittings from two SWNT reactive sites, each site measured at a different potential. Fitting the titrations from many reactive sites gives the distributions of the kinetic constants at the corresponding potentials (Figure 6B−E, G−J). Regardless of the applied potential, the distributions of the rate constants are broad relative to their average values, indicating the large reactivity heterogeneity among these reactive sites. As k_2^{red}, k_3^{ox}, and k_4^{red} all involve electron transfer, these rate constants are related to the electronic properties of the SWNT reactive sites. Therefore, the broad distributions of k_2^{red}, k_3^{ox}, and k_4^{red} reflect the variable electronic properties among these discrete reactive sites, which could be due to the different chemical nature of these sites, or to the different electronic properties of SWNTs (e.g., metallic or semiconducting). Nevertheless, as the SWNTs are deposited on the ITO surface nonspecifically in our electrochemical flow cell (Figure 2A), the electrical contact with the ITO may vary from one SWNT to another, which could also contribute to the observed reactivity heterogeneity. Future experiments using metal electrodes evaporated directly onto the SWNTs will help minimize contact variability.[19]

The distributions of k_2^{red}, k_3^{ox}, and k_4^{red} are expectedly dependent on the applied potential, as they all involve electron transfer. With the potential going from −0.1 to −0.35 V, the average values of k_2^{red} and k_4^{red} increase (Figure 6C,E,H,J), consistent with their being electro-reduction reactions (Figure 5C), whereas the average value of k_3^{ox} decreases (Figure 6D,I), consistent with its being an electro-oxidation reaction (Figure 5C). Interestingly, the average value of k_1 is also dependent on the potential (Figure 6B,G), indicating that the potential also plays a role in the replacement of $\mathbf{PH_2}$ from a SWNT reactive site by **S** (Figure 5C). Detailed study in the future of the potential dependence of

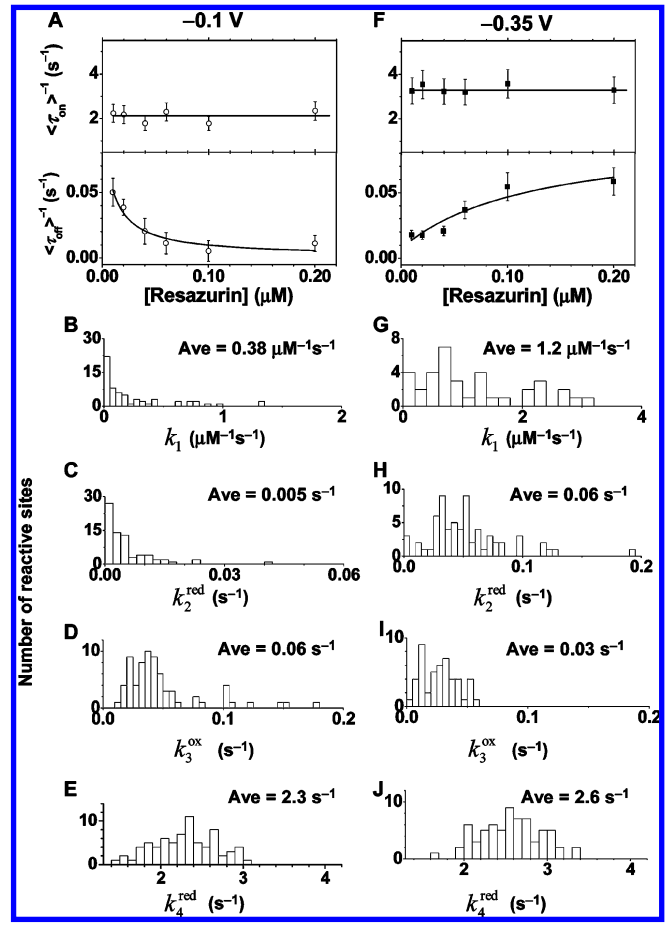

Figure 6. Heterogeneity of electrocatalytic reactivity of SWNT reactive sites. (A,F) Resazurin concentration dependence of $\langle\tau_{on}\rangle^{-1}$ and $\langle\tau_{off}\rangle^{-1}$ of two reactive sites, one at −0.1 V (A) and the other at −0.35 V (F). Error bars in the graphs are SEM. Solid lines are fits with eqs 1 and 2. For the reactive site at −0.1 V, $k_1 = 0.1 \pm 0.8\ \mu M^{-1}s^{-1}$, $k_2^{red} = 0.001 \pm 0.006\ s^{-1}$, $k_3^{ox} = 0.11 \pm 0.07\ s^{-1}$, $k_4^{red} = 2.1 \pm 0.1\ s^{-1}$. For the reactive site at −0.35 V, $k_1 = 0.8 \pm 0.6\ \mu M^{-1}s^{-1}$, $k_2^{red} = 0.09 \pm 0.04\ s^{-1}$, $k_3^{ox} = 0.01 \pm 0.01\ s^{-1}$, $k_4^{red} = 3.3 \pm 0.1\ s^{-1}$. Errors are SD. (B−E, G−J) Distributions of kinetic rate constants of many SWNT reactive sites at −0.1 V (B−E) and −0.35 V (G−J).

these rate constants, in particular k_2^{red}, k_3^{ox}, and k_4^{red}, may provide insight into the underlying interfacial electron-transfer kinetics between a SWNT and an adsorbed molecule.

In summary, we demonstrate single-molecule fluorescence microscopy of SWNT electrocatalysis at single-reaction resolution. The wide-field imaging allows multiplexed observation of electrocatalysis by many SWNTs in real time. We found that the electrocatalytic reactions occur at discrete, nanometer-dimension reactive sites on the SWNTs, where the enhanced mass transport allows measurements of steady-state electrochemical electron-transfer kinetics. We formulated a kinetic mechanism for the observed electrocatalytic reactions, and determined the associated kinetic rate constants for each SWNT reactive site. The distributions of the rate constants reveal large reactivity heterogeneity among the SWNT reactive sites, which likely reflect their heterogeneous electronic properties following from their different chemical nature or from different SWNT electronic properties. In combination with electrical conductance measurements that

directly probe the electronic property of SWNTs,[3−7] this single-molecule fluorescence method should be powerful to interrogate how the electronic structure of SWNTs affects the kinetics of electron-transfer across a solid−liquid interface, which is a fundamental issue in photoelectrochemical cells, batteries, and fuel cells and for which single-molecule techniques can offer unique insights.[37−43,58,59]

Acknowledgment. We thank ACS PRF and NSF-funded Cornell Center for Materials Research for funding.

Supporting Information Available: Materials and methods, additional results, and analyses. This material is available free of charge via the Internet at http://pubs.acs.org.

References

(1) Iijima, S.; Ichihashi, T. *Nature (London)* **1993**, *363*, 603.
(2) *Carbon Nanotubes*; Endo, M., Iijima, S., Dresselhaus, M. S., Eds.; Elsevier Science, Inc.: New York, 1996.
(3) Colbert, D. T.; Smalley, R. E. *Trends Biotechnol.* **1999**, *17*, 4–50.
(4) Lu, W.; Lieber, C. M. *Nat. Mater.* **2007**, *6*, 841–850.
(5) Dekker, C. *Phys. Today* **1999**, *52*, 22–28.
(6) McEuen, P. L. *Phys. World* **2000**, *13*, 31–36.
(7) Dai, H. *Acc. Chem. Res.* **2002**, *35*, 1035–1044.
(8) Katz, E.; Willner, I. *ChemPhysChem* **2004**, *5*, 1084–1104.
(9) Goldsmith, B. R.; Coroneus, J. G.; Kane, A. A.; Weiss, G. A.; Collins, P. G. *Nano Lett.* **2008**, *8*, 189–194.
(10) Barone, P. W.; Jeng, E. S.; Heller, D. A.; Strano, M. S. In *Handbook of Biosensors and Biochips*; Marks, R. S., Lowe, C. R., Cullen, D. C., Weetall, H. H., Karube, I, Eds.; John Wiley and Sons: Chichester, 2007; Vol. 2, pp 843−854.
(11) Carlson, L. J.; Krauss, T. D. *Acc. Chem. Res.* **2008**, *41*, 235–243.
(12) Cumings, J.; Zettl, A. In *Applied Physics of Carbon Nanotubes: Fundamentals of Theory, Optics and Transport Devices*; Rotkin, S. V., Subramoney, S., Eds.; Springer: Berlin, 2005, 273–306.
(13) *Carbon Nanotubes: Synthesis, Structure, Properties, and Applications*; Dresselhaus, M. S., Dresselhaus, G., Avouris, P., Eds.; Springer: Berlin, 2000.
(14) Odom, T. W.; Huang, J.-L.; Kim, P.; Lieber, C. M. *Nature (London)* **1998**, *391*, 62–64.
(15) Tans, S. J.; Verschueren, A. R. M.; Dekker, C. *Nature (London)* **1998**, *393*, 49–52.
(16) Wildoer, J. W. G.; Venema, L. C.; Rinzler, A. G.; Smalley, R. E.; Dekker, C. *Nature (London)* **1998**, *391*, 59–62.
(17) Hersam, M. C. *Nat. Nanotechnol.* **2008**, *3*, 387–394.
(18) Campbell, J. K.; Sun, L.; Crooks, R. M. *J. Am. Chem. Soc.* **1999**, *121*, 3779–3780.
(19) Heller, I.; Kong, J.; Heering, H. A.; Williams, K. A.; Lemay, S. G.; Dekker, C. *Nano Lett.* **2005**, *5*, 137–142.
(20) Heller, I.; Kong, J.; Williams, K. A.; Dekker, C.; Lemay, S. G. *J. Am. Chem. Soc.* **2006**, *128*, 7353–7359.
(21) Gooding, J. J. *Electrochim. Acta* **2005**, *50*, 3049–3060.
(22) McCreery, R. *Chem. Rev.* **2008**, *108*, 2646–2687.
(23) Bard, A. J.; Faulkner, L. R. *Electrochemical Methods: Fundamentals and Applications*, 2nd ed.; John Wiley & Sons, Inc.: New York, 2000.
(24) Zhang, J.; Liu, X.; Blume, R.; Zhang, A.; Schloegl, R.; Su, D. S. *Science* **2008**, *322*, 73–77.
(25) Goldsmith, B. R.; Coroneus, J. G.; Khalap, V. R.; Kane, A. A.; Weiss, G. A.; Collins, P. G. *Science* **2007**, *315*, 77–81.
(26) Fan, Y.; Goldsmith, B. R.; Collins, P. G. *Nat. Mater.* **2005**, *4*, 908–911.
(27) Gong, K.; Du, F.; Xia, Z.; Durstock, M.; Dai, L. *Science* **2009**, *323*, 760–764.
(28) Chi, K. R. *Nat. Methods* **2009**, *6*, 15–18.
(29) Hell, S. W. *Nat. Methods* **2009**, *6*, 24–32.
(30) Betzig, E.; Patterson, G. H.; Sougrat, R.; Lindwasser, O. W.; Olenych, S.; Bonifacino, J. S.; Davidson, M. W.; Lippincott-Schwartz, J.; Hess, H. F. *Science* **2006**, *313*, 1642–1645.
(31) Rust, M. J.; Bates, M.; Zhuang, X. *Nat. Methods* **2006**, *3*, 793–796.
(32) Hess, S. T.; Girirajan, T. P. K.; Mason, M. D. *Biophys. J.* **2006**, *91*, 4258–4272.
(33) Sharonov, A.; Hochstrasser, R. M. *Proc. Natl. Acad. Sci. U.S.A.* **2006**, *103*, 18911–18916.
(34) Biteen, J. S.; Thompson, M. A.; Tselentis, N. K.; Bowman, G. R.; Shapiro, L.; Moerner, W. E. *Nat. Methods* **2008**, *5*, 947–949.
(35) Bates, M.; Huang, B.; Zhuang, X. *Curr. Opin. Chem. Biol.* **2008**, *12*, 505–514.
(36) Heilemann, M.; Linde, S. v. d.; Schüttpelz, M.; Kasper, R.; Seefeldt, B.; Mukherjee, A.; Tinnefeld, P.; Sauer, M. *Angew. Chem., Int. Ed.* **2008**, *47*, 6172–6176.
(37) Palacios, R. E.; Fan, F.-R. F.; Bard, A. J.; Barbara, P. F. *J. Am. Chem. Soc.* **2006**, *128*, 9028–9029.
(38) Bard, A. J. *ACS Nano* **2008**, *2*, 2437–2440.
(39) Chang, Y.-L.; Palacios, R. E.; Fan, F.-R. F.; Bard, A. J.; Barbara, P. F. *J. Am. Chem. Soc.* **2008**, *130*, 8906–8907.
(40) Palacios, R. E.; Fan, F.-R. F.; Grey, J. K.; Suk, J.; Bard, A. J.; Barbara, P. F. *Nat. Mater.* **2007**, *6*, 680–685.
(41) Fan, F.-R. F.; Bard, A. J. *Nano Lett.* **2008**, *8*, 1746–1749.
(42) Lei, C.; Hu, D.; Ackerman, E. J. *Chem. Commun.* **2008**, 5490–5492.
(43) Lei, C.; Hu, D.; Ackerman, E. *Nano Lett.* **2009**, *9*, 655–658.
(44) Twigg, R. S. *Nature (London)* **1945**, *155*, 401–402.
(45) Xu, W.; Kong, J. S.; Yeh, Y.-T. E.; Chen, P. *Nat. Mater.* **2008**, *7*, 992–996.
(46) Xu, W.; Kong, J. S.; Chen, P. *Phys. Chem. Chem. Phys.* **2009**, *11*, 2767–2778.
(47) Chen, P.; Xu, W.; Zhou, X.; Panda, D.; Kalininskiy, A. *Chem. Phys. Lett.* **2009**, *470*, 151–157.
(48) Hu, H.; Zhao, B.; Itkis, M. E.; Haddon, R. C. *J. Phys. Chem. B* **2003**, *107*, 13838–13842.
(49) Yu, A.; Bekyarova, E.; Itkis, M. E.; Fakhrutdinov, D.; Webster, R.; Haddon, R. C. *J. Am. Chem. Soc.* **2006**, *128*, 9902–9908.
(50) Rosenblatt, S.; Yaish, Y.; Park, J.; Gore, J.; Sazonova, V.; McEuen, P. L. *Nano Lett.* **2002**, *2*, 869–872.
(51) Bates, M.; Huang, B.; Dempsey, G. T.; Zhuang, X. *Science* **2007**, *317*, 1749–1753.
(52) Huang, B.; Wang, W.; Bates, M.; Zhuang, X. *Science* **2008**, *319*, 810–813.
(53) Thompson, R. E.; Larson, D. R.; Webb, W. W. *Biophys. J.* **2002**, *82*, 2775–2783.
(54) Yildiz, A.; Forkey, J. N.; McKinney, S. A.; Ha, T.; Goldman, Y. E.; Selvin, P. R. *Science* **2003**, *300*, 2061–2065.
(55) Huang, H.; Maruyama, R.; Noda, K.; Kajiura, H.; Kadono, K. *J. Phys. Chem. B* **2006**, *106*, 7316–7320.
(56) Xie, X. S. *Single Mol.* **2001**, *2*, 229–236.
(57) Xu, W.; Kong, J. S.; Chen, P. *J. Phys. Chem. C* **2009**, *113*, 2393–2404.
(58) Fan, F.-R. F.; Kwak, J.; Bard, A. J. *J. Am. Chem. Soc.* **1996**, *118*, 9669–9675.
(59) Wang, Y.; Wang, X.; Ghosh, S. K.; Lu, H. P. *J. Am. Chem. Soc.* **2009**, *131*, 1479–1487.

NL900988F